

See discussions, stats, and author profiles for this publication at: <https://www.researchgate.net/publication/233406002>

Insight into the Correlation between Net Topology and Ligand Coordination Mode in New Lanthanide MOFs Heterogeneous Catalysts: A Theoretical and Experimental Approach

ARTICLE in CRYSTAL GROWTH & DESIGN · SEPTEMBER 2012

Impact Factor: 4.89 · DOI: 10.1021/cg301096d

CITATIONS

15

READS

35

6 AUTHORS, INCLUDING:



Richard Fernando D'vries

University of São Paulo

21 PUBLICATIONS 152 CITATIONS

SEE PROFILE



Victor Antonio de la Peña O'Shea

Madrid Institute for Advanced Studies

75 PUBLICATIONS 1,255 CITATIONS

SEE PROFILE



Enrique Gutiérrez-Puebla

Instituto de Ciencia de Materiales de Madrid

346 PUBLICATIONS 6,103 CITATIONS

SEE PROFILE



Angeles Monge

Spanish National Research Council

441 PUBLICATIONS 6,747 CITATIONS

SEE PROFILE

Insight into the Correlation between Net Topology and Ligand Coordination Mode in New Lanthanide MOFs Heterogeneous Catalysts: A Theoretical and Experimental Approach

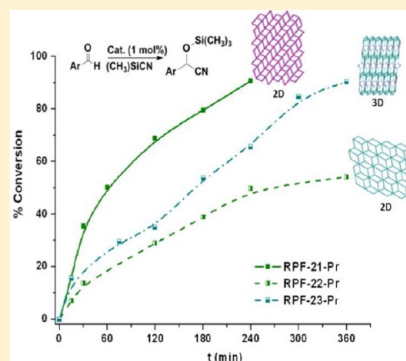
Richard F. D'Vries,[†] Víctor A. de la Peña-O'Shea,[‡] Natalia Snejko,[†] Marta Iglesias,[†] Enrique Gutiérrez-Puebla,[†] and M. Ángeles Monge^{*,†}

[†]Instituto de Ciencia de Materiales de Madrid (ICMM-CSIC), Cantoblanco 28049, Madrid, Spain

[‡]Thermochemical Process Group, Instituto Madrileño de Estudios Avanzados en Energía (IMDEA Energía), Avenida Ramon de la Sagra n 3, 28935 Mostoles, Spain

S Supporting Information

ABSTRACT: Three new families of compounds were obtained as pure phases, with different lanthanide cations and the 3,5-disulfobenzoic acid (3,5-DSB). The hydrothermal synthesis conditions' influence on structural type obtained was studied. The structural type RPF-21 corresponds to the compound $[\text{Ln}(3,5\text{-DSB})(\text{H}_2\text{O})_5]$ ($\text{Ln} = \text{La}, \text{Pr}, \text{Nd}$); RPF-22 to the compound $[\text{Ln}(3,5\text{-DSB})(\text{H}_2\text{O})_3]$ ($\text{Ln} = \text{La}, \text{Pr}, \text{Nd}, \text{Sm}, \text{and Eu}$), and RPF-23 to the compound $[\text{Ln}_3(3,5\text{-DSB})_2(\text{OH})_3(\text{H}_2\text{O})_3]$ ($\text{Ln} = \text{Pr}, \text{Nd}, \text{and Eu}$). The dimensionality and the topology of the compounds are determined by the sulfonate group coordination modes; RPF-23 presents a new type of topology. Computational studies have determined the relative energies for those compounds that coexist under certain hydrothermal conditions, and they have brought some light to the thermodynamic or kinetic control that drives each reaction. The new materials were tested as catalysts in cyanosilylation reaction (CSR) of aldehydes under solvent-free conditions. The three of them catalyze the CSRs within 4 h, and a remarkable difference in activity is found between RPF-21 and the other two materials. The catalytic activity mainly depends on the network structure, with very little influence of the lanthanide cation. The mechanism includes, probably, a displacement of the catalyst labile water molecules by aldehyde before catalyst's activation and reaction.



INTRODUCTION

The chemistry of metal organic frameworks (MOFs) has been developed now sufficiently enough to arrive at a point where the main variants and necessary components for MOFs synthesis are more or less clearly established. The practice of MOFs synthesis testifies that by selecting properly metal cations and adequate ligand type we can control to a large extent the connectivity of metal ions and ligand functional groups, MOF topology, and, generally speaking, the design of certain MOF structures. Still, the process of MOF crystals formation during hydrothermal or solvothermal synthesis needs special attention in order to understand and estimate the main factors that influence the kinetic and thermodynamic components of the MOFs crystallization process and, thus, to advance the so much needed understanding of the composition–structure–property relationships in MOFs.

Among the most studied MOFs properties are optical properties,¹ magnetic behavior,² gas absorption,³ drug delivery,⁴ and catalytic behavior.⁵ These properties are closely associated with the structure, the topology, and the nature of the metallic cation and ligand.⁶ It is to be mentioned that lanthanide compounds are among the most promising catalysts and are being studied extensively in the past few years.^{5a,c,7} Previously, we have reported the synthesis, structure, and studies of the

catalytic properties of some lanthanide MOFs (most of them RPFs = rare earth polymeric frames) that have been demonstrated to possess excellent catalytic activity.^{5a,c,6b,8} Continuing our research, in this paper, we present a series of lanthanide compounds ($\text{Ln} = \text{La}, \text{Pr}, \text{Nd}, \text{Sm}, \text{and Eu}$) with the 3,5-disulfobenzoic acid (3,5-DSB), which forms MOFs of three different structures and topologies promoted by different coordination modes of sulfonate and carboxylate groups of the 3,5-DSB ligand. The dependence was studied of the type of the structures obtained vs the synthetic approach utilized. The catalytic activity toward solvent-free cyanosilylation reaction was tested for the compounds produced; in addition, the reactivity was studied as a function of the structure, the metallic cation, and the type of the substrate.

EXPERIMENTAL SECTION

General Information. All reagents and solvents employed were commercially available and used as supplied without further purification: 3,5-disulfobenzoic acid, disodium salt (98% Sigma-Aldrich); $\text{Ln}(\text{NO}_3)_3 \cdot 6\text{H}_2\text{O}$ ($\text{Ln} = \text{La}, \text{Pr}, \text{Nd}, \text{and Sm}$; all 99%

Received: August 1, 2012

Revised: September 11, 2012

Published: September 14, 2012

Strem Chemicals); $\text{Eu}(\text{NO}_3)_3 \cdot 6\text{H}_2\text{O}$ (99% Acros Organics). The IR spectra were recorded from KBr pellets in the range $4000\text{--}250\text{ cm}^{-1}$ on a Bruker IFS 66 V/S. The thermogravimetric and differential thermal analyses (TGA-DTA) were performed using Seiko TG/DTA 320U equipment in a temperature range between 25 and $1000\text{ }^\circ\text{C}$ in air (100 mL/min flow) with a heating rate of $10\text{ }^\circ\text{C}/\text{min}$. A Perkin-Elmer CNHS Analyzer 2400 was employed for the elemental analysis.

Synthesis. Three RPF-21-Ln with formula $[\text{Ln}(\text{3,5-DSB})(\text{H}_2\text{O})_5]$ (Ln = La, Pr, Nd) were synthesized under the same reaction conditions. For the Pr compound, 0.075 g (0.23 mmol) of 3,5-DSB Na_2 was added to a solution of $\text{Pr}(\text{NO}_3)_3 \cdot 6\text{H}_2\text{O}$ (0.1 g, 0.23 mmol) in water (6 mL); subsequently, an aqueous solution of sodium hydroxide (1 mol/L) was dropwise added, adjusting the pH value of the initial reaction mixture to $\sim 6\text{--}7$. The mixture was then magnetically stirred at room temperature for 5 min and afterward was transferred to a Teflon-lined stainless steel autoclave and heated at $170\text{ }^\circ\text{C}$ for 24 h. After the mixture was cooled to room temperature, the crystalline product was filtered and washed with water and acetone. As mentioned above, using the same procedure, La and Nd compounds were obtained. Elemental analysis: calculated for La ($\text{C}_7\text{H}_{13}\text{O}_{13}\text{S}_2\text{La}$): C, 16.54; H, 2.58; S, 12.61. Found: C, 16.68; H, 2.54; S, 11.81. Calculated for Pr ($\text{C}_7\text{H}_{13}\text{O}_{13}\text{S}_2\text{Pr}$): C, 16.48; H, 2.57; S, 12.56. Found: C, 16.49; H, 2.43; S, 12.06. Calculated for Nd ($\text{C}_7\text{H}_{13}\text{O}_{13}\text{S}_2\text{Nd}$): C, 16.37; H, 2.55; S, 12.49. Found: C, 16.24; H, 2.44; S, 11.34.

RPF-22-Ln. $[\text{Ln}(\text{3,5-DSB})(\text{H}_2\text{O})_3]$ (Ln = La, Pr, Nd, Sm, and Eu). For the Pr compound, 3,5-DSB Na_2 (0.075 g, 0.23 mmol) was added to a solution of $\text{Pr}(\text{NO}_3)_3 \cdot 6\text{H}_2\text{O}$ (0.1 g, 0.23 mmol) in water (6 mL); an aqueous solution of sodium hydroxide (1 mol/L) was dropwise added, adjusting the pH value to ~ 7 , and magnetically stirred at room temperature for 5 min. The resultant reaction mixture was transferred to a Teflon-lined stainless steel autoclave and heated at $200\text{ }^\circ\text{C}$ for 24 h. After the mixture was cooled to room temperature, the crystalline product was filtered and washed with water and acetone. The same procedure was used for the synthesis of the La, Nd, and Sm compounds. Elemental analysis: calculated for La ($\text{C}_7\text{H}_9\text{O}_{11}\text{S}_2\text{La}$): C, 17.81; H, 1.92; S, 13.58. Found: C, 17.29; H, 1.63; S, 12.50. Calculated for Pr ($\text{C}_7\text{H}_9\text{O}_{11}\text{S}_2\text{Pr}$): C, 17.73; H, 1.91; S, 13.52. Found: C, 17.74; H, 1.77; S, 13.31. Calculated for Nd ($\text{C}_7\text{H}_9\text{O}_{11}\text{S}_2\text{Nd}$): C, 17.61; H, 1.90; S, 13.43. Found: C, 17.60; H, 2.07; S, 12.58. Calculated for Sm ($\text{C}_7\text{H}_9\text{O}_{11}\text{S}_2\text{Sm}$): C, 17.38; H, 1.88; S, 13.26. Found: C, 15.56; H, 1.54; S, 12.23. Calculated for Eu ($\text{C}_7\text{H}_9\text{O}_{11}\text{S}_2\text{Eu}$): C, 17.33; H, 1.87; S, 13.22. Found: C, 16.81; H, 1.73; S, 12.87.

Using the same reaction conditions as for RPF-22-Ln but augmenting the time of the hydrothermal reaction up to 3 days, RPF-23-Ln $[\text{Ln}_3(\text{3,5-DSB})_2(\text{OH})_3(\text{H}_2\text{O})_3]$ (Ln = Pr, Nd, and Eu) were obtained. Elemental analysis: calculated for Pr ($\text{C}_{14}\text{H}_{15}\text{O}_{22}\text{S}_4\text{Pr}_3$): C, 15.48; H, 1.39; S, 11.80. Found: C, 15.61; H, 1.52; S, 11.09. Calculated for Nd ($\text{C}_{14}\text{H}_{15}\text{O}_{22}\text{S}_4\text{Nd}_3$): C, 15.34; H, 1.38; S, 11.70. Found: C, 15.3; H, 1.51; S, 12.36. Calculated for Eu ($\text{C}_{14}\text{H}_{15}\text{O}_{22}\text{S}_4\text{Eu}_3$): C, 15.02; H, 1.35; S, 11.46. Found: C, 16.87; H, 1.63; S, 11.11.

Single-Crystal Structure Determination. Single-crystal X-ray data for all compounds were obtained in a Bruker-Siemens Smart CCD diffractometer equipped with a normal focus and with a 2.4 kW sealed tube X-ray source (Mo $K\alpha$ radiation = 0.71073 \AA) operating at 50 kV and 30 mA. Data were collected over a hemisphere of the reciprocal space by a combination of three sets of exposure. Each exposure of 20 s covered 0.3° in ω . The unit cell dimensions were determined for least-squares fit of reflections with $I > 20\sigma$. The structures were solved by direct methods. The final cycles of refinement were carried out by full-matrix least-squares analyses with anisotropic thermal parameters of all non-hydrogen atoms. The hydrogen atoms were fixed at their calculated positions using distances and angle constraints. All calculations were performed using SMART software for data collection,⁹ SAINT for data reduction,¹⁰ and SHELXTL to resolve and refine the structure.¹¹

X-ray Powder Diffraction. Powder X-ray diffraction (PXRD) patterns were measured with a Bruker D8 diffractometer, with step size = 0.02° and exposure time = 0.5 s/step. X-ray powder diffraction

measurements were used to check the purity of the obtained microcrystalline products by comparison of the experimental results with the simulated patterns obtained from single crystal X-ray diffraction data. The residues of the compounds after TG analyses were analyzed by X-ray powder diffraction and compared with the ICSD patterns reported.

Computational Details. Ab-initio calculations were performed by plane-wave density functional (PW-DF) calculations using the VASP package.¹² The energy is calculated by employing the generalized gradient approximation, in particular, the exchange and correlation functional of Perdew and Wang (PW91).¹³ The effect of the core electrons on the valence electron density was described by the projector augmented wave (PAW) method.¹⁴ The cutoff for the kinetic energy of the plane waves has been set to 415 eV throughout, which after extensive test proved to ensure a total energy convergence better than 10^{-6} eV. Geometry optimization on selected starting geometries obtained from single-crystal X-ray diffraction (see corresponding experimental details) was carried out using a gradient-conjugate method. The apparent formation energy was calculated as an energy difference between the corresponding reagents and MOFs structures.

Catalytic Study. The detailed reaction conditions are shown in the captions of Tables 2 and 3 and Scheme 2. The cyanosilylation reaction of aldehydes was carried out at $40\text{ }^\circ\text{C}$. Into a Pyrex-glass screw cap vial (volume: ca. 10 mL) were successively placed catalyst (5 mg, 1 mol %) and aldehyde (1 mmol), in the absence of solvent. A Teflon-coated magnetic stir bar was added, and the reaction was initiated by addition of trimethylsilyl cyanide, TMS-CN (1.5 mmol). The reaction mixture was vigorously stirred (800 rpm) at $40\text{ }^\circ\text{C}$ under N_2 atmosphere. The progress of the reaction was monitored by GC analysis. After the reaction was completed, the solid was removed by centrifugation of the reaction mixture. All products (cyanohydrin trimethylsilyl ethers) were identified by comparison of their GC retention times, GC-MS spectra, and/or ^1H and ^{13}C NMR spectra with those of authentic data. GC analysis was performed using Konik HRGC 4000B GCMS with a cross-linked (95%)-dimethyl-(5%)-diphenylpolysiloxane (Teknokroma TRB-SMS) column of 30 m.

Recycling Experiment. The reuse experiment was carried out for the cyanosilylation of benzaldehyde. The reaction was carried out under the standard conditions. After the reaction was completed (more than 90% conversion, 240 min), the catalyst was recovered by filtration (4.3 mg, 86% recovery), washed with acetone, and air-dried prior to being used for the reuse experiment. The PXRD pattern of the retrieved catalyst was identical to that of the fresh (Supporting Information Figure S5). In addition, the recovered catalyst can be reused for cyanosilylation of benzaldehyde without an appreciable loss of its high catalytic performance. When the cyanosilylation of benzaldehyde was carried out with the recovered catalyst under the standard conditions, cyanohydrin trimethylsilyl ether was obtained in 91% yield (in 240 min).

RESULTS AND DISCUSSION

Effect of Synthesis Conditions. In order to obtain pure phases in the system $\text{Ln}^{3+}\text{--}3,5\text{-DSB}$, several synthetic experiments were carried out. Different compounds were obtained by hydrothermal reaction of a stoichiometric (1:1) mixture of reactants. The reaction variables were the temperature and time. First, it was found that at temperatures lower than $170\text{ }^\circ\text{C}$ no product was formed. When performing the synthesis at $170\text{ }^\circ\text{C}$ during 24 h, RPF-21-Ln structural type (ST) with formula $[\text{Ln}(\text{3,5-DSB})(\text{H}_2\text{O})_5]$ (Ln = La, Pr and Nd) is obtained as a pure phase. By increasing the reaction temperature up to $200\text{ }^\circ\text{C}$, $[\text{Ln}(\text{3,5-DSB})(\text{H}_2\text{O})_3]$ (Ln = La, Pr, Nd, Sm, and Eu) with RPF-22-Ln ST comes up as a unique phase in 24 h. However, when performing the synthesis at these last conditions during 3 days, a new more condensed phase is obtained as the only reaction product: $[\text{Ln}_3(\text{3,5-DSB})_2(\text{OH})_3(\text{H}_2\text{O})_3]$ (Ln = Pr, Nd, Eu), RPF-23-Ln, with Ln/DSB ratio = $3/2$. To understand

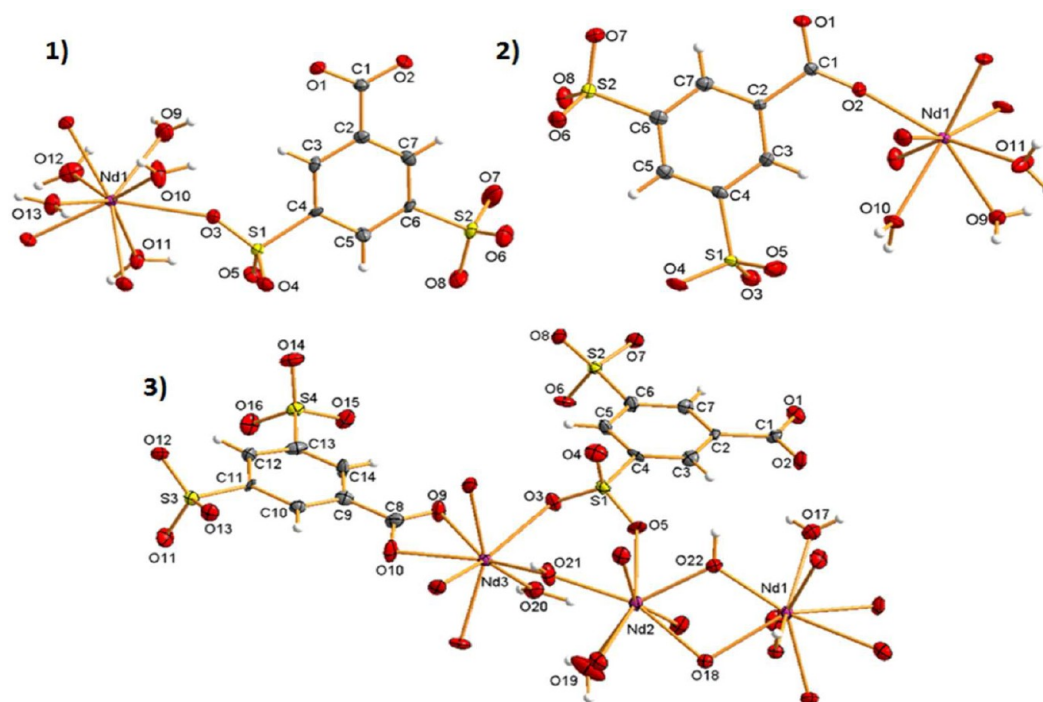


Figure 1. ORTEP drawing of the asymmetric units for (1) RPF-21-Nd, (2) RPF-22-Nd, and (3) RPF-23-Nd; ellipsoids are displayed at the 50% probability level.

better the process, more experiments were performed, and the results are shown in Figure 10, right, and in Supporting Information Figure S2. The increase of the reaction time provokes a decrease in the coordinated water molecules number and augments coordination of the ligand sulfonate groups to the metallic center (RPF-21 and RPF-22 are 2D structures). When increasing the temperature, the more condensed (RPF-23) 3D structure is obtained in a shorter period of time.

Structural Analysis. Figure 1 shows the asymmetric units (AU) for the three structural types. The main crystallographic and refinement data are given in Table 1.

RPF-21-Ln is a series of isostructural compounds with formula $[\text{Ln}(3,5\text{-DSB})(\text{H}_2\text{O})_5]$ (Ln = La, Pr, and Nd) that crystallizes in the triclinic space group $P\bar{1}$. In this structural type, the metallic centers are nine-coordinated to five water molecules, two carboxylate groups, and two sulfonate groups, forming LnO_9 trigonal prism square-face tricapped polyhedra (TPRS-9).¹⁵ The (3,5-DSB) linker joints the PBUs through the carboxylate, and one of the sulfonate groups along the $[010]$ and $[001]$ directions, respectively, acting thus, in a $\eta^2\mu_2$ mode for both connections (Scheme 1, Figure 2). This arrangement gives rise to layers in the plane (011).

The layer can be topologically described as a uninodal 4-connected net type $\text{sql}/\text{Shubnikov tetragonal plan}^{16}$ with point (Schläfli) symbol $(4^4\cdot 6^2)$, where the nodal point is sited either at the metallic center position or at the ligand middle point of the C–S line (Figure 3).

The supramolecular 3D structure is formed mainly through hydrogen bonds, that link the covalent layers forming a three-dimensional supramolecular net. This net can be topologically explained by the connection of the uncoordinated sulfonate group with a coordinated water molecule of the adjacent layer, at a distance $\text{O9} \cdots \text{H9B} \cdots \text{O7}$ of 2.77(1), 2.75(2), and 2.760(6) Å for La, Pr, and Nd, respectively. Only the strongest

hydrogen bond, which gives dimensionality to the net along the $[100]$ direction, was considered in the topological study. With these new connections, the nodes extend their connectivity to five, and the resultant network is a uninodal 5-connected net with the point (Schläfli) symbol $(4^6\cdot 6^4)$ for the net and topological type $\text{bnn hexagonal BN } (5/4/h5; \text{sqc}12)^{13}$ (Figure 4).

RPF-22 structural type, with formula $[\text{Ln}(3,5\text{-DSB})(\text{H}_2\text{O})_3]$ (Ln = La, Pr, Nd, Sm, and Eu). The lanthanide cation is octacoordinated to three water molecules and five ligand oxygen atoms in a LnO_8 dodecahedron. As it happens in RPF-21, the carboxylate and one sulfonate group of the 3,5-DSB are both $\eta^2\mu_2$ coordinated; however, the remaining sulfonate group that was free in the latter acts in a η^1 mode in RPF-22. This connectivity gives rise to a bidimensional array in the (110) plane. The *anti-anti* disposition of the sulfonate groups and the $\eta^2\mu_2$ mode of the carboxylate group allow the formation of $\text{LnO}_8\text{--C}_2\text{--LnO}_8$ paddle wheel SBUs, which grow along $[100]$ thanks to the sulfonate group $\text{SBU--S}_2\text{--SBU}$ connections. Along the $[010]$ direction, the whole ligands link these chains developing the layer. This arrangement forces the superposition of the aromatic rings and stacking interactions (Figure 5) with distances between centroids of 3.4778(3), 3.5087(5), 3.5339(4), and 3.6036(3) for Eu, Nd, La, and Pr, respectively.

The layers can be topologically explained as a uninodal 5-connected net (the ligand also links five metallic centers, 5-coordinated nodes) of the type SP 2-periodic net (6,3)IIa with point (Schläfli) symbol $(4^8\cdot 6^2)$ (Figure 6).

In this structural type the 3D supramolecular arrangement between layers is driven, as in RPF-21, by hydrogen bonds. The strongest hydrogen interaction is between a water molecule and a sulfonate oxygen with $\text{O9} \cdots \text{H9A} \cdots \text{O7}$ distances 2.739(7), 2.781(9), and 2.725(5) Å for La, Pr, and Nd, respectively. This interaction increases the net dimensionality by connecting the layers along the $[001]$ direction. As a result of these

Table 1. Crystal and Refinement Data for RPF-21-Ln, RPF-22-Ln, and RPF-23-Ln

compd	RPF-21-La	RPF-21-Pr	RPF-21-Nd	RPF-22-La	RPF-22-Pr	RPF-22-Nd	RPF-22-Sm	RPF-22-Eu	RPF-23-Pr	RPF-23-Nd	RPF-23-Eu
empirical formula	C ₇ H ₁₃ O ₁₃ S ₂ La	C ₇ H ₁₃ O ₁₃ S ₂ Pr	C ₇ H ₁₃ O ₁₃ S ₂ Nd	C ₇ H ₉ O ₁₁ S ₂ La	C ₇ H ₉ O ₁₁ S ₂ Pr	C ₇ H ₉ O ₁₁ S ₂ Nd	C ₇ H ₉ O ₁₁ S ₂ Sm	C ₇ H ₉ O ₁₁ S ₂ Eu	C ₁₄ H ₁₅ O ₂₂ S ₄ Pr ₃	C ₁₄ H ₁₅ O ₂₂ S ₄ Nd ₃	C ₁₄ H ₁₅ O ₂₂ S ₄ Eu ₃
FW	508.22	510.22	513.55	472.19	474.19	477.52	483.64	485.25	1086.27	1096.26	1119.45
crystal system	triclinic	triclinic	triclinic	triclinic	triclinic	triclinic	triclinic	triclinic	triclinic	triclinic	triclinic
space group	<i>P</i> $\bar{1}$	<i>P</i> $\bar{1}$	<i>P</i> $\bar{1}$	<i>P</i> $\bar{1}$	<i>P</i> $\bar{1}$	<i>P</i> $\bar{1}$	<i>P</i> $\bar{1}$	<i>P</i> $\bar{1}$	<i>P</i> $\bar{1}$	<i>P</i> $\bar{1}$	<i>P</i> $\bar{1}$
unit cell dimensions											
<i>a</i> (Å)	7.985(4)	7.9374(6)	7.9189(6)	6.8605(7)	6.815(4)	6.8018(9)	6.7756(9)	6.7596(6)	7.0037(2)	6.9851(12)	6.9288(3)
<i>b</i> (Å)	10.350(5)	10.2921(7)	10.2672(7)	9.2706(9)	9.212(5)	9.1664(13)	9.1132(13)	9.0967(8)	11.0535(4)	11.0348(18)	10.9662(4)
<i>c</i> (Å)	10.744(5)	10.6569(7)	10.6272(8)	11.5362(14)	11.495(6)	11.4643(16)	11.4212(16)	11.4061(9)	17.6185(6)	17.554(3)	17.3785(6)
α (deg)	115.937(8)	115.969(1)	115.991(1)	113.595(1)	113.405(8)	113.368(2)	113.234(2)	113.188(1)	77.823(1)	77.849(3)	77.930(1)
β (deg)	93.647(9)	93.303(1)	93.174(1)	92.819(2)	93.228(9)	93.384(2)	93.672(2)	93.763(1)	82.173(1)	82.221(3)	82.473(1)
γ (deg)	105.354(8)	105.368(1)	105.360(1)	104.617(1)	104.536(8)	104.466(2)	104.411(2)	104.385(1)	75.604(1)	75.530(3)	75.645(1)
volume (Å ³)	753.4(6)	739.40(9)	734.12(9)	641.21(12)	631.1(6)	625.21(15)	617.13(15)	613.88(9)	1286.33(7)	1275.9(4)	1246.58(8)
<i>Z</i>	2	2	2	2	2	2	2	2	2	2	2
ρ_{calc} (mg/m ³)	2.241	2.292	2.323	2.446	2.495	2.537	2.603	2.625	2.805	2.853	2.982
abs coef (mm ⁻¹)	3.179	3.645	3.889	3.714	4.249	4.545	5.155	5.508	46.868	6.445	7.896
<i>F</i> (000)	704	500	502	456	460	462	466	468	1032	1038	1056
θ range for data collection (deg)	2.15–25.03	2.33–28.29	2.32–26.37	1.95–25.03	1.96–28.28	1.97–26.37	2.47–26.37	1.98–26.37	2.58–62.12	1.19–25.02	1.95–25.03
reflections collected/unique	4178/2424	7687/3642	6179/2923	4851/2222	6325/3040	5139/2474	5299/2494	5239/2471	14315/3974	9217/4376	9154/4268
[<i>R</i> (int)]	[0.0398]	[0.0456]	[0.0418]	[0.0332]	[0.0256]	[0.0289]	[0.0232]	[0.0295]	[0.1304]	[0.0366]	[0.0268]
completeness (%)	90.5	98.9	98	98.5	97.1	96.4	98.7	98.3	98.1	96.9	96.8
data/restraints/params	2424/0/202	3642/0/202	2923/0/210	2222/0/214	3040/0/190	2474/0/190	2494/0/215	2471/0/198	3974/0/329	4376/0/322	4268/0/388
goodness-of-fit on <i>F</i> ²	1.215	1.071	1.052	1.110	1.266	1.071	1.064	1.086	1.483	1.266	1.276
<i>R</i> 1 [<i>I</i> > 2 σ (<i>I</i>)]	0.0538, 0.1256	0.0446, 0.0918	0.0380, 0.0809	0.0351, 0.0693	0.0345, 0.0771	0.0292, 0.0635	0.0207, 0.0493	0.0280, 0.0689	0.0879, 0.2517	0.0655, 0.1833	0.0400, 0.0970
<i>wR</i> 2 [<i>I</i> > 2 σ (<i>I</i>)]	0.0577, 0.1270	0.0696, 0.1053	0.0485, 0.0843	0.0431, 0.0715	0.0368, 0.0780	0.0360, 0.0656	0.0234, 0.0503	0.0308, 0.0702	0.2196, 0.3488	0.0753, 0.1903	0.0529, 0.1150
<i>wR</i> 2 (all data)	1.609 and	3.135 and	0.974 and	0.561 and	0.960 and	1.239 and	0.965 and	0.857 and	5.363 and	3.162 and	3.313 and
largest diff peak and hole	–2.026	–1.795	–0.933	–1.441	–2.951	–1.072	–0.891	–1.586	–6.195	–2.823	–1.845

Scheme 1. Representation of Coordination Modes for the 3,5-DSB Ligand in RPF-21, RPF-22, and RPF-23

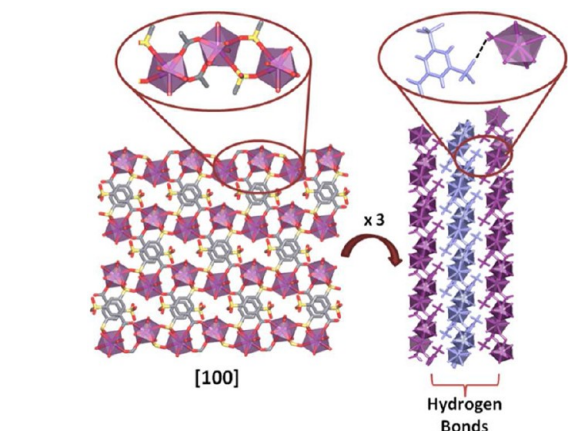
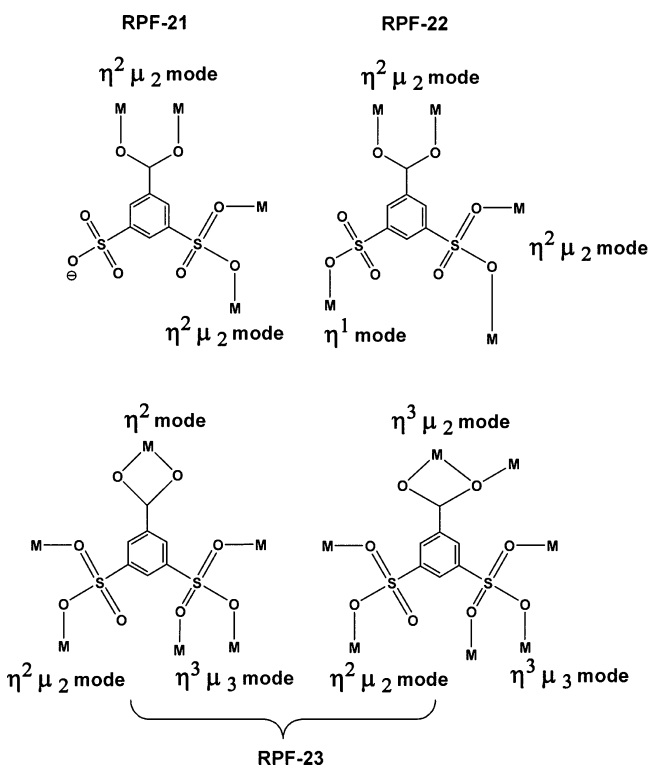


Figure 2. RPF-21 (left) view of the layers along the [100] direction; (right) view of the hydrogen bonds between layers along [001].

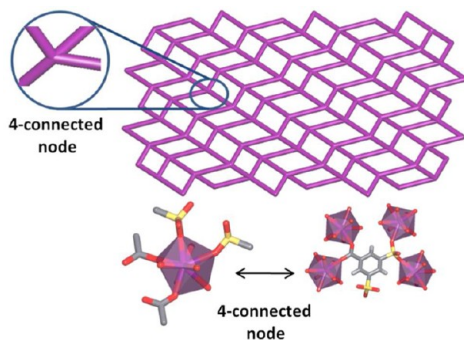


Figure 3. RPF-21: Topological representation as a 4-connected Shubnikov tetragonal plane.

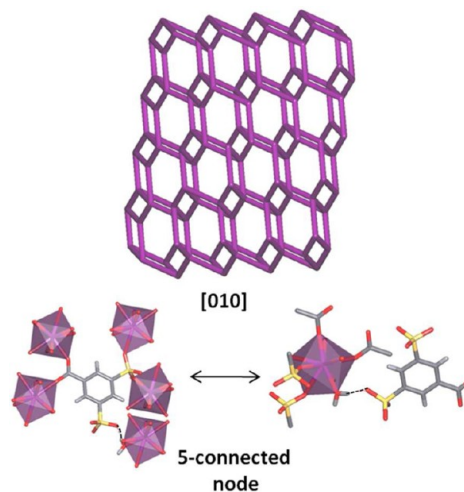


Figure 4. RPF-21: Topological representation of the supramolecular net as a 5-connected bnn hexagonal net.

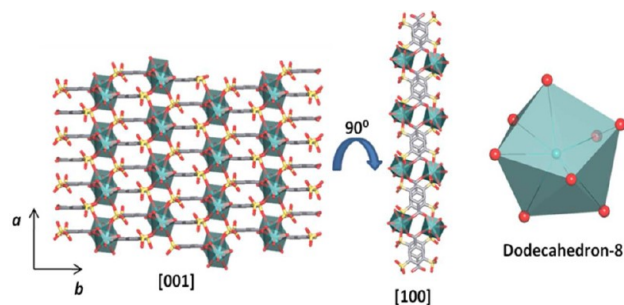


Figure 5. RPF-22: (left) view of the layer along the [001] and [100] directions; (right) polyhedral representation of the metal environment.

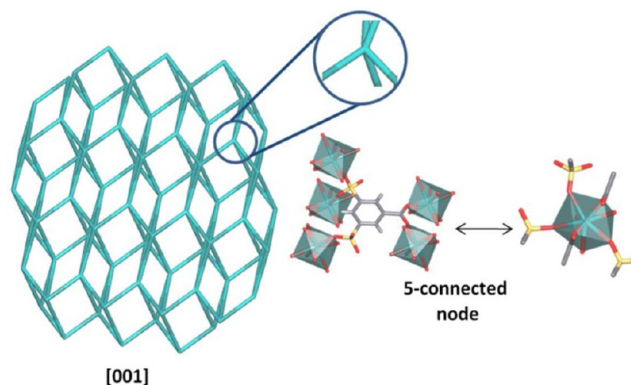


Figure 6. RPF-22: Topological representation of the 5-connected SP 2-periodic net (6,3)IIa.

connections, the supramolecular net can be topologically explained as a 6-connected uninodal net of type 6/4/ $t7(sqc885)$, with point (Schläfli) symbol $(4^{11}.6^4)$ (Figure 7).

RPF-23-Ln compounds possess the formula $[Ln_3(3,5-DSB)_2(OH)_3(H_2O)_3]$ (Ln = Pr, Nd, Eu). The asymmetric unit is formed by three different metallic centers. Two of them, Ln2 and Ln3, octacoordinated, form trigonal prism square-face bicapped polyhedra, while the third one (Ln1), nine-coordinated, is at the center of a trigonal prism square-face tricapped polyhedron.¹⁵ The asymmetric unit also comprises two crystallographically independent ligands, three hydroxyl groups, and three coordinated water molecules. The Ln3

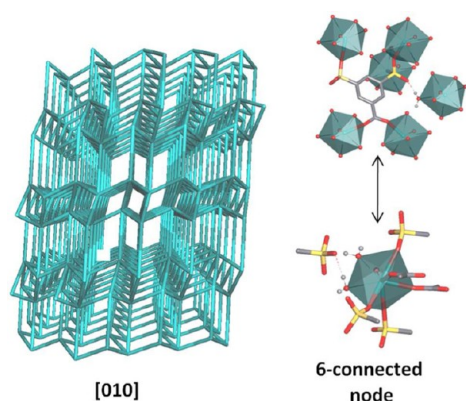


Figure 7. RPF-22: Topological representation of the supramolecular net as a 6-connected type sqc885 network.

coordination environment consists of four sulfonate oxygen atoms, two chelate carboxylate oxygen atoms, one hydroxyl group, and one water molecule. Ln2 is coordinated to three sulfonate oxygen atoms, three hydroxyl groups, one carboxylate oxygen atom, and one water molecule. Finally, the Ln1 cation is coordinated to three sulfonate oxygen atoms, three hydroxyl groups, two chelate carboxylate oxygen atoms, and one water molecule. Six-polyhedra secondary building units (SBUs) are formed by junction of one central sharing edge $[\text{Ln}_4(\mu_3\text{-OH})_2(\mu\text{-OH})_4(\text{H}_2\text{O})_4(\text{O}_{\text{cb}})_4(\text{O}_{\text{sf}})_{12}]$ (cb = carboxylate, sf = sulfonate) tetranuclear cluster, which is formed thanks to the presence of two $\mu_3\text{-OH}^-$, two $\mu_2\text{-OH}^-$, two $\eta^3\mu_2$ oxo-carboxylates, and two more terminal polyhedra (Ln3) in such a way that the SBU formula is $[\text{Ln}_6(\mu_3\text{-OH})_2(\mu\text{-OH})_4(\text{H}_2\text{O})_6(\text{O}_{\text{cb}})_8(\text{O}_{\text{sf}})_{20}]$ (Figure 8).

The two anions of the multitopic 3,5-DSB ligands, whose sulfonate groups act in both $\eta^3\mu_3$ and $\eta^2\mu_2$ modes, differ in the carboxylate coordination mode, since they act as η^2 in one of them and as $\eta^3\mu_2$ in the other (Scheme 1). The SBUs are linked

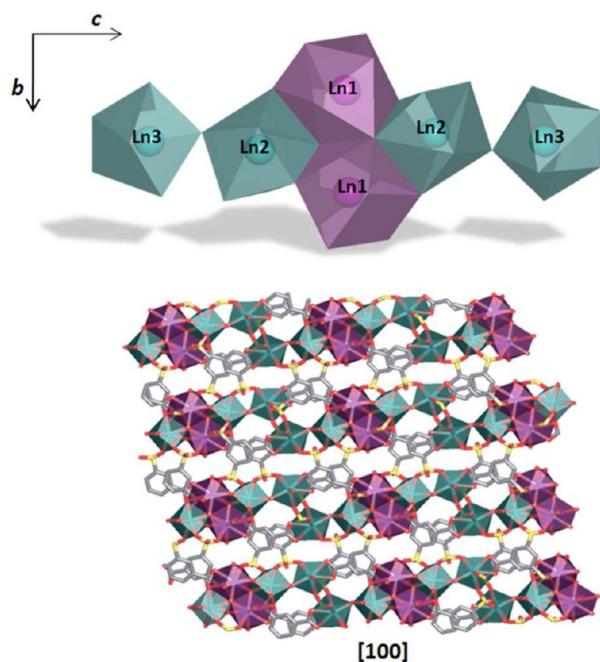


Figure 8. RPF-23: (top) polyhedral representation of the SBU; (bottom) view of the network along the [100] direction.

along the [100] and [001] directions through the $\eta^3\mu_3$ and $\eta^2\mu_2$ sulfonate groups, respectively, giving rise to infinite inorganic layers in the plane (101) junctions among layers made *via* the whole ligand.

The topological simplification of this complex 3D net is quite complicated, and it has been done as follows: the central cluster $[\text{Ln}_4(\text{OH})_4]^{8+}$ and the $[\text{Ln}_n(\text{SO}_3)_n]_n$ chains along the [010] direction have been taken separately. The central cluster can be simplified as a 12-connected node, while the Ln atoms involved in the chains are considered as 6-connected nodes, with the two ligand centroids being depicted as 6- and 4-connected nodes (Figure 9). With this simplification the network is a new four

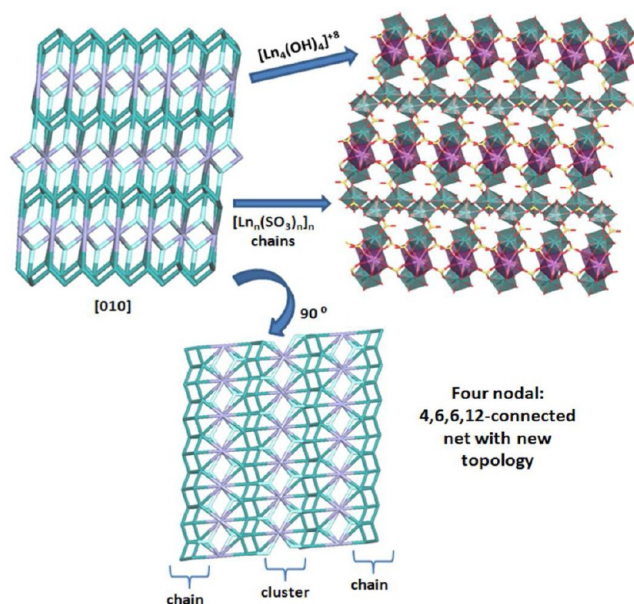


Figure 9. Polyhedral and topological representations of RPF-23 along the [010] and [100] directions.

nodal net, with the point (Schläfli) symbol $(3^2 \cdot 4^8 \cdot 5^3 \cdot 6^2)2(3^4 \cdot 4^{20} \cdot 5^{14} \cdot 6^{25} \cdot 8^3)(4^6)2$. It is worth pointing out that the topology the RPF-23 net exhibits is a new topology and, thus, is not registered in any database yet.

Two or more structural types appear along the studied lanthanide series: the La compound adopts the RPF-21 and RPF-22 STs; the Pr compound comes up with RPF-21, RPF-22, and RPF-23 STs; the Sm compound only accepts the RPF-22 ST; Eu can appear with RPF-22 or RPF-23 STs so that the *bridge* lanthanide between two structural types can exhibit, besides its own structural type, those of the two adjacent lanthanides. The only found exception in this series is the Sm compound, which should adopt the RPF-23 ST too, but until now there is no evidence or trace of its presence in any of the performed reactions. It has to be noticed that when the synthesis temperature is lowered to 170 °C for Sm and Eu, another phase appears (under study now).

IR Spectra. The RPF-21-Ln compounds present the same IR profile. Symmetric and antisymmetric OH stretching bands appears as a broad band at 3550 cm^{-1} . The C–H vibrations belonging to the aromatic rings of the 3,5-DSB ligand are found around $\sim 3050\text{--}3100\text{ cm}^{-1}$. The bands present at ~ 1570 and 1610 cm^{-1} are assigned to $\nu_{\text{as}}(\text{OCO})$ vibrations, and the bands at ~ 1390 and $\sim 1440\text{ cm}^{-1}$ are associated with the symmetric $\nu_{\text{s}}(\text{OCO})$ mode. S=O and S–O vibrations are observed in the region of $\sim 1040\text{--}1130\text{ cm}^{-1}$ and are related with the

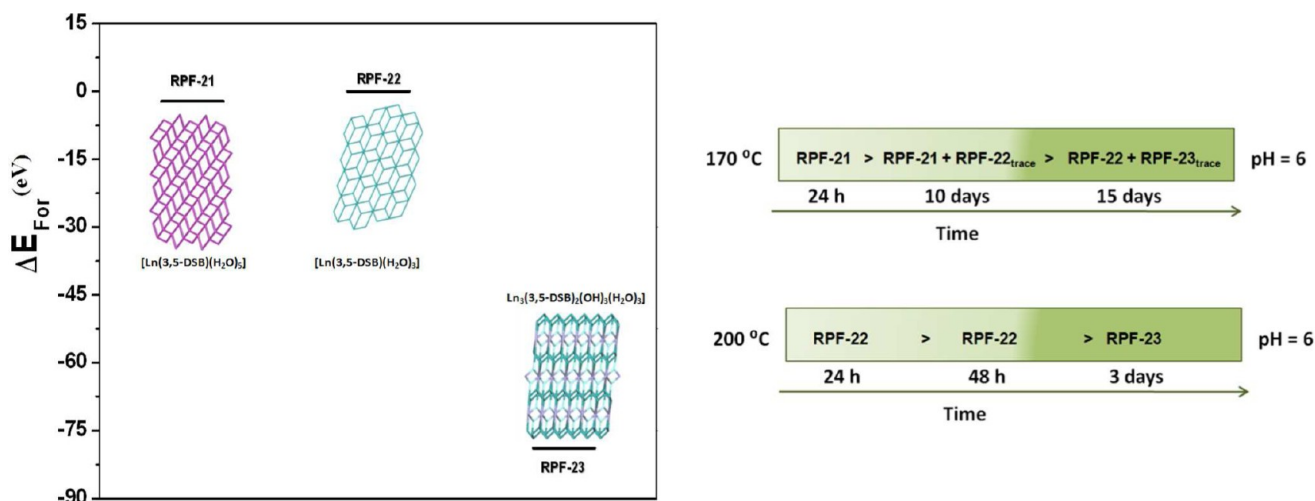


Figure 10. (left) Calculated formation energies. (right) Summary of the hydrothermal conditions for compounds RPF-21, RPF-22, and RPF-23.

coordinated sulfonate group.¹⁷ In this region we can also find four bands characteristic of the bridged bidentate sulfonate group ($\eta^2\mu_2$). The band around $\sim 435\text{ cm}^{-1}$ is assigned to M–O vibrations (Supporting Information Figure S2). Although compounds RPF-21, RPF-22, and RPF-23 are different structurally, they have similar vibrational spectra, and the same spectral profile inside compounds' families. OH stretching bands are present in the region $3200\text{--}3600\text{ cm}^{-1}$ for both RPF-22 and RPF-23 compounds. The C–H ring vibrations are observed at $\sim 3060\text{--}3100\text{ cm}^{-1}$. For S=O and S–O, four bands in the region of $1050\text{--}1130\text{ cm}^{-1}$ in the spectra of RPF-22 are broader than in the case of RPF-21, due to the presence of $\eta^2\mu_2$ and η^1 coordination modes in the RPF-22-Ln; in RPF-23-Ln, only three bands are present in the same region for the combination of $\eta^2\mu_2$ and $\eta^3\mu_3$ modes.¹⁷

Thermal Study. The thermogravimetric analysis for the RPF-21, RPF-22, and RPF-23 compounds shows them to be stable thermally up to $500\text{ }^\circ\text{C}$. Compound RPF-21-Ln presents a mass loss of the coordinated water molecules in three stages: at ~ 70 , ~ 130 , and $\sim 160\text{ }^\circ\text{C}$. The total decomposition of the structure begins at $\sim 540\text{ }^\circ\text{C}$, and the final product found was $(\text{LnO})_2\text{SO}_4$ [ICSD 66823].¹⁸

Compound RPF-22-Ln presents a mass loss of three coordinated water molecules around $\sim 110\text{--}150\text{ }^\circ\text{C}$ depending on the metallic cation. For all compounds, the decomposition begins at $\sim 530\text{ }^\circ\text{C}$ with the final formation of $(\text{LnO})_2\text{SO}_4$.¹⁸

The thermal decomposition of compounds RPF-23-Ln begins with the gradual mass loss corresponding to coordinated water molecules at $\sim 140\text{ }^\circ\text{C}$, followed by the decomposition of the ligand at $\sim 460\text{ }^\circ\text{C}$ approximately, with the same decomposition product as in the above cases.

Theoretical Stability Studies. Previous works have shown that theoretical calculations are a powerful tool to determine the factors that govern the mechanisms of MOFs formation.¹⁹

This work also confirmed the important role that the synthesis conditions play in the structural properties of the obtained organo–inorganic frameworks. With the aim to determine and understand the factors that have influence in this experimental behavior, a series of theoretical PW-DF calculations were carried out. As the new praseodymium materials exhibit three structural types, these element compounds were chosen to perform the structural stability study and carry out comparisons. In all cases, the geometry

optimization converged to a stable structure with the same topology as that determined experimentally, even though no symmetry constraints were imposed.

Taking into account the results coming from formation energies (Figure 10), several conclusions can be drawn. First, the RPF-23 phase presents the lowest formation energy (E_{For}), while, for RPF-21 and RPF-22, the energetic stability is almost the same. This fact and the experimental results indicate that at shorter reaction times and low temperature the reaction is kinetically controlled, obtaining for short periods of time RPF-21 and RPF-22, while at longer reaction times RPF-22 is obtained, along with traces of the most stable phase.

With the temperature increasing ($200\text{ }^\circ\text{C}$), the reaction obeys a kinetic control, but the obtained phase is RPF-22, with slightly higher energy than RPF-21. This behavior is due to the fact that, by increasing the reaction temperature, a reduction in the number of coordinate water molecules and a higher coordination of the ligand sulfonate groups to the metallic center is provoked. This water lost leads to the formation of the RPF-22 phase at the beginning of the reaction and to the most stable phase RPF-23, with 3D structure, at longer periods of time.

Catalytic Study. Cyanosilylation reactions (CSRs) are important C–C bond-forming reactions that are catalyzed by Lewis acids and Lewis acids/bases.²⁰ In coordination polymers, vacant coordination site(s) on the metal and/or functional organic sites for possible interactions with reactants have been reported to be involved in catalysis of these reactions.²¹ In the cyanosilylation reaction, methodologies which involve the utilization of homogeneous, heterogeneous, or enzymatic catalysts have been widely studied.²² Many of them involve high cost or high difficulty to separate the final product. Therefore, this paper is addressed to the creation of new metal–organic framework catalysts for cyanosilylation reactions under soft conditions, low catalyst charge, and solvent-free conditions.

First of all, the reaction conditions were established as follows: $T = 40\text{ }^\circ\text{C}$, 1 mol % of catalyst, in the absence of solvent and using the benzaldehyde as model substrate. Second, the three praseodymium compounds belonging to the RPF-21, RPF-22, and RPF-23 frameworks were tested on it as catalysts with the following results: The three of them catalyze the CSRs within 4 h (Scheme 2 and Table 2); however, a remarkable

Scheme 2. Catalytic Cyanosilylation of Various Aldehydes

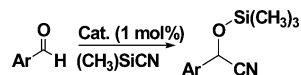


Table 2. RPF Compounds as Catalysts for Cyanosilylation of Benzaldehyde

	time (h)	yield (%) ^a	TOF (h ⁻¹) ^b	dimensionality	topology	coord. no.
RPF-21-Pr	4	90.7	78.8	2D	sql/Shubnikov tetragonal plane	9
RPF-22-Pr	6	54	10.2	2D	SP 2-periodic net (6,3)IIa	8
RPF-23-Pr	6	90.3	13.8	3D	new topology	8, 9
RPF-21-La	4	93.2	71.2	2D	sql/Shubnikov tetragonal plane	9
RPF-21-Nd	4	89.2	73	2D	sql/Shubnikov tetragonal plane	9

^aYield determined by GC-MS. ^bTOF: %Conv (mmol of substrate / mmol cat.).

difference in activity was found between RPF-21 and the other two structural types (Figure 11). Once the kinetic profiles and the reactivity ratio of the three different compounds were known, the influence of the metal center in the reactivity was also studied in RPF-21-Ln (La, Pr, and Nd). As can be seen in Figure 12 and Table 2, the metal center does not have a significant influence on the reactivity.

As a result of these tests, and taking into account the net topologies, the coordination number of the metals, and the dimensionality of the nets (Table 2), some conclusions can be extracted: (i) The activity depends mainly on the network structure. (ii) For RPF-21, which bears the Ln cation with the highest coordination number, and thus less vacant positions, with five of the nine positions occupied by water molecules, it seems quite plausible that the reaction proceeds via displacement of the labile water by aldehyde before its activation and reaction (Scheme 3). (iii) In the case of RPF-22 and -23 the

possible mechanism follows the same water displacement, but the lability of the molecule depends on the metallic center saturation, following the order of coordination number RPF-21 (CN = 9) > -23 (CN = 8, 9) > -22 (CN = 8).

In a next step, the relation of the substrate nature and the catalyst reactivity was also studied for RPF-21-Pr, with the results showed in Figure 13. The conversion decreases in the order 4-methylbenzaldehyde (99%) > benzaldehyde (90%) > 4-fluorobenzaldehyde (70%), in line with their corresponding electronic effects. Some tests were also performed with aliphatic aldehydes, showing higher reactivity for the heptanal than for the citral (Table 3); these latter results could indicate some steric effect, too (Figure 13).

Recycling Test. To probe the heterogeneity of the catalysts, after the catalytic reactions, all the compounds were recovered from their reaction media. The solids were isolated, washed, and analyzed to confirm the maintenance of the structure by powder X-ray diffraction (Supporting Information Figure S6). Specifically for compound RPF-21-Pr, this procedure was realized at least four times, without loss of catalytic activity and keeping the structure and the crystallinity after the last experiment, as can be seen in Figure 14. These series of new compounds are applicable heterogeneous active catalysts.

CONCLUSIONS

Eleven new compounds, belonging to three new structural types, have been obtained as pure phases, with different lanthanide cations and the 3,5-DSB ligand. From the explored hydrothermal synthesis conditions it can be established that the increase of the reaction time leads to higher coordination of the ligand sulfonate groups to the metallic center, and to a reduction in the coordinated water molecules number.

Two or more structural types appear along the studied lanthanide element series: the La compound adopts the RPF-21 and RPF-22 STs; the Pr compound comes up with RPF-21, RPF-22, and RPF-23 STs; the Sm compound only accepts the RPF-22 ST; Eu can appear with RPF-22 or RPF-23 STs so that the bridge lanthanide between two structural types can even exhibit, besides its own structural type, those of the two

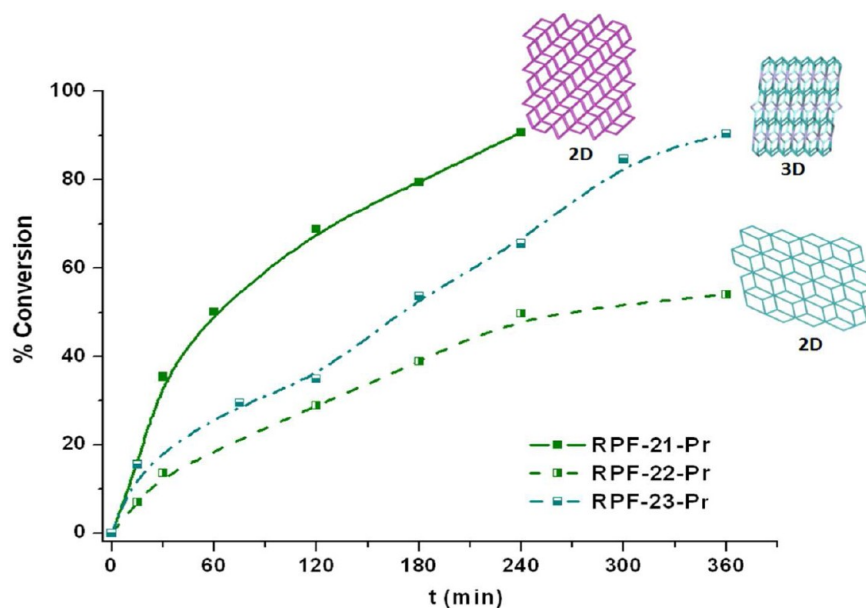


Figure 11. Kinetic profile for the cyanosilylation of benzaldehyde with the RPF-21-Pr, RPF-22-Pr, and RPF-23-Pr as catalysts.

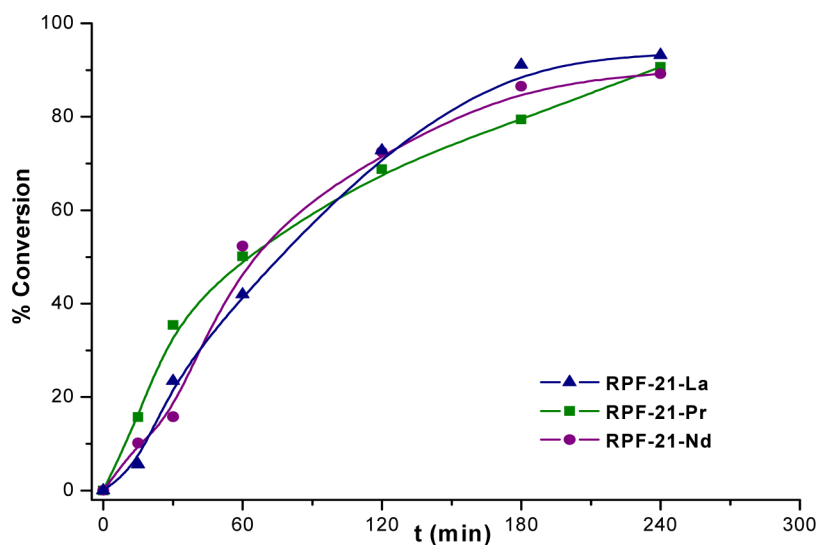


Figure 12. Kinetic profile for the benzaldehyde cyanosilylation reaction catalyzed by the isostructural compounds RPF-21-Ln (Ln = La, Pr, and Nd).

Scheme 3. Proposed Mechanism for the Cyanosilylation Reaction in the Case of RPF-21

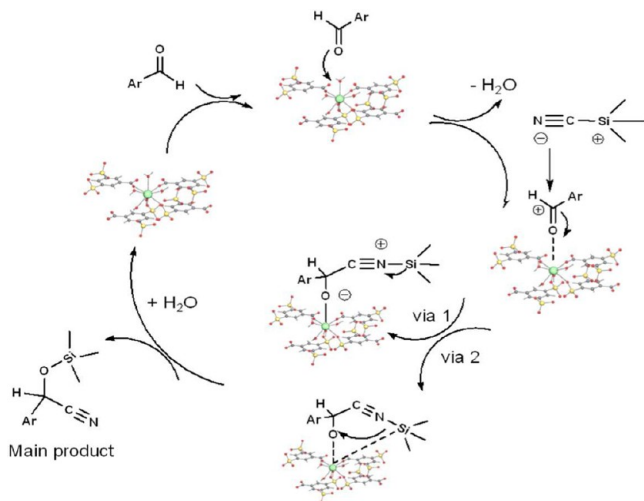


Table 3. Scope of RPF-Pr-21-Catalyzed Cyanosilylation of Aldehydes

Substrate	Time (h)	Yield (%)
	7	80.3
	0.5	99
	24	86.1
	2	96.7
	24	82.8

adjacent lanthanides. The only found exception in this series is the Sm compound, which should adopt the RPF-23 ST too, but until now there is no evidence of its presence in any of the performed reactions.

The topological analysis of the compounds shows three different networks, which directly depend on the ligand coordination modes. It is remarkable that one of the three topological nets (that of RPF-23) is a new four nodal net, with $(3^2 \cdot 4^7 \cdot 5^4 \cdot 6^2)2(3^2 \cdot 4^8 \cdot 5^3 \cdot 6^2)2(3^4 \cdot 4^{20} \cdot 5^{14} \cdot 6^{25} \cdot 8^3)(4^6)2$ point (Schläfli) symbol; it has not been reported in any database yet.

Computational studies have determined the relative energies for the three structural types that coexist under certain hydrothermal conditions, and they have brought some light to the thermodynamic or kinetic control that drives each reaction.

The new materials were tested as catalysts in cyanosilylation reaction of aldehydes under solvent-free conditions. The three of them catalyze the CSRs within 4 h, and a remarkable difference in activity was found between RPF-21 and the other two structural types. The activity mainly depends on the network structure, with very little influence of the lanthanide cation, and very probably, the reaction goes via displacement of the labile water molecules by aldehyde before catalyst activation and reaction.

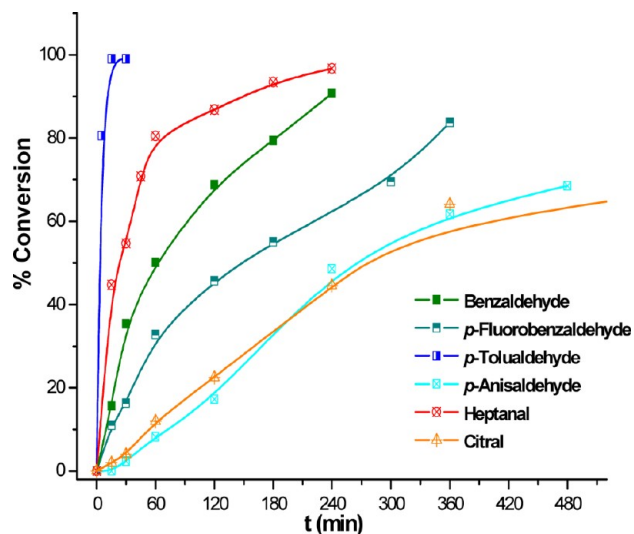


Figure 13. Kinetic profiles for the RPF-21-Pr-catalyzed cyanosilylation of aldehydes.

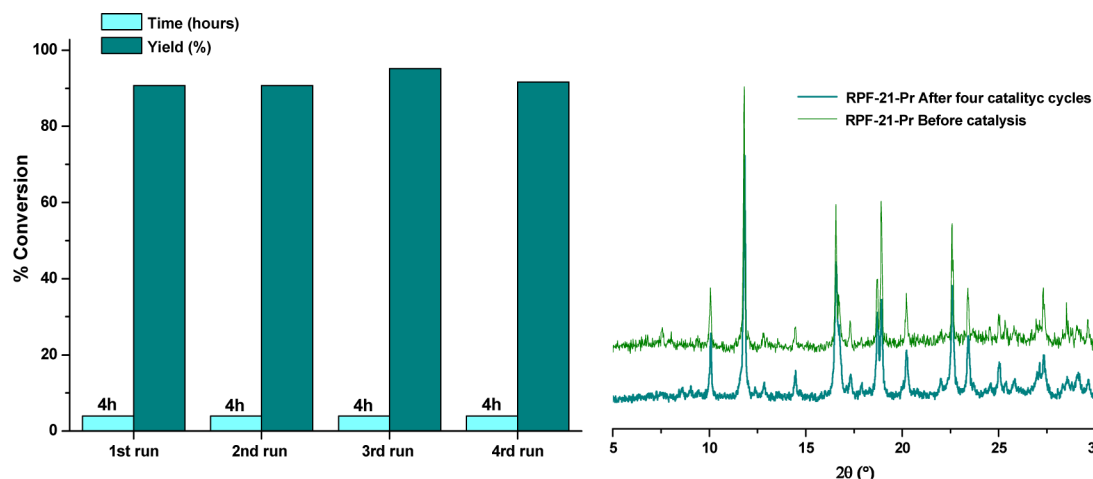


Figure 14. (left) Recyclability of compound RPF-21-Pr. (right) X-ray pattern comparison before and after four catalytic cycles.

■ ASSOCIATED CONTENT

Supporting Information

Experimental and simulated powder X-ray diffraction patterns for RPF-21, RPF-22, and RPF-23. Powder X-ray diffraction pattern comparison of RPF-22 and RPF-23 with the product after 10 and 15 days of reaction. FT-IR spectroscopy, thermal gravimetric analysis, and X-ray powder patterns after TG analysis and after catalysis for RPF-21, RPF-22, and RPF-23. This material is available free of charge via the Internet at <http://pubs.acs.org>. CCDC reference numbers 889096–889106 contain the supplementary crystallographic data for this paper. This data can be obtained free of charge from the Cambridge Crystallographic Data Centre via www.ccdc.cam.ac.uk/data_request/cif.

■ AUTHOR INFORMATION

Corresponding Author

*E-mail: amonge@icmm.csic.es.

Notes

The authors declare no competing financial interest.

■ ACKNOWLEDGMENTS

The authors thank Prof. Davide Proserpio for his valuable advice on the topology studies. R.F.D. acknowledges a FPI scholarship from the Spanish Ministry of Economy and Competitiveness (MINECO), and Fondo Social Europeo from the EU. This work has been supported by the Spanish MCYT Projects MAT2010-17571, MAT2011-29020-C02-02, FAMA S2009/MAT-1756 Comunidad Autónoma de Madrid, and Consolider-Ingenio CSD2006-2001. V.A.P.-O. acknowledges financial support from the MCYT in the Ramon y Cajal Program and ENE2009-09432. Computational time has been provided by the Centre de Supercomputació de Catalunya (CESCA) and the Centro de Supercomputación de Galicia (CESGA).

■ REFERENCES

- (1) (a) Harbuzaru, B. V.; Corma, A.; Rey, F.; Atienzar, P.; Jordá, J. L.; García, H.; Ananias, D.; Carlos, L. D.; Rocha, J. *Angew. Chem., Int. Ed.* **2008**, *47*, 1080. (b) Gándara, F.; Andrés, A. d.; Gómez-Lor, B.; Gutiérrez-Puebla, E.; Iglesias, M.; Monge, M. A.; Proserpio, D. M.; Snejko, N. *Cryst. Growth Des.* **2008**, *8*, 378.
- (2) (a) Srikanth, H.; Hajndl, R.; Moulton, B.; Zaworotko, M. J. *J. Appl. Phys.* **2003**, *93*, 7089. (b) Snejko, N.; Gutiérrez-Puebla, E.;

Martínez, J. L.; Monge, M. A.; Ruiz-Valero, C. *Chem. Mater.* **2002**, *14*, 1879. (c) MasPOCH, D.; Ruiz-Molina, D.; Wurst, K.; Domingo, N.; Cavallini, M.; Biscarini, F.; Tejada, J.; Rovira, C.; Veciana, J. *Nat. Mater.* **2003**, *2*, 190. (d) Rao, C. N. R.; Cheetham, A. K.; Thirumurugan, A. *J. Phys.: Condens. Matter* **2008**, *20*, 083202.

(3) (a) Furukawa, H.; Ko, N.; Go, Y. B.; Aratani, N.; Choi, S. B.; Choi, E.; Yazaydin, A. Ö.; Snurr, R. Q.; O'Keeffe, M.; Kim, J.; Yaghi, O. M. *Science* **2010**, *329*, 424. (b) Perles, J.; Iglesias, M.; Ruiz-Valero, C.; Snejko, N. *J. Mater. Chem.* **2004**, *14*, 2683.

(4) (a) McKinlay, A. C.; Morris, R. E.; Horcajada, P.; Férey, G.; Gref, R.; Couvreur, P.; Serre, C. *Angew. Chem., Int. Ed.* **2010**, *49*, 6260. (b) Huxford, R. C.; Della Rocca, J.; Lin, W. *Curr. Opin. Chem. Biol.* **2010**, *14*, 262.

(5) (a) Lee, J.; Farha, O. K.; Roberts, J.; Scheidt, K. A.; Nguyen, S. T.; Hupp, J. T. *Chem. Soc. Rev.* **2009**, *38*, 1450. (b) Gándara, F.; Puebla, E. G. r.; Iglesias, M.; Proserpio, D. M.; Snejko, N.; Monge, M. A. n. *Chem. Mater.* **2009**, *21*, 655. (c) Corma, A.; García, H.; Llabrés i Xamena, F. X. *Chem. Rev.* **2010**, *110*, 4606.

(6) (a) Yoon, M.; Srirambalaji, R.; Kim, K. *Chem. Rev.* **2011**, *112*, 1196. (b) Monge, A.; Gandara, F.; Gutierrez-Puebla, E.; Snejko, N. *CrystEngComm* **2011**, *13*, 5031.

(7) Dhakshinamoorthy, A.; Alvaro, M.; Garcia, H. *Catal. Sci. Technol.* **2011**, *1*, 856.

(8) (a) D'Vries, R. F.; Iglesias, M.; Snejko, N.; Alvarez-Garcia, S.; Gutierrez-Puebla, E.; Monge, M. A. *J. Mater. Chem.* **2012**, *22*, 1191.

(b) Medina, M. E.; Platero-Prats, A. E.; Snejko, N.; Rojas, A.; Monge, A.; Gándara, F.; Gutiérrez-Puebla, E.; Cambor, M. A. *Adv. Mater.* **2011**, *23*, 5283. (c) Gándara, F.; Perles, J.; Snejko, N.; Iglesias, M.; Gómez-Lor, B.; Gutiérrez-Puebla, E.; Monge, M. A. *Angew. Chem., Int. Ed.* **2006**, *45*, 7998. (d) Jiang, H.-L.; Xu, Q. *Chem. Commun.* **2011**, *47*, 3351. (e) Ma, L.; Abney, C.; Lin, W. *Chem. Soc. Rev.* **2009**, *38*, 1248.

(9) SMART, V 5.04 ed.; Bruker-Siemens: Madison, WI.

(10) SAINT, V 6.28A ed.; Bruker-Siemens: Madison, WI.

(11) SHELXTL, V 5.1 ed.; Bruker-Siemens: Madison, WI.

(12) (a) Kresse, G.; Furthmüller, J. *Comput. Mater. Sci.* **1996**, *6*, 15. (b) Kresse, G.; Hafner, J. *Phys. Rev. B* **1993**, *47*, 558.

(13) (a) Perdew, J. P.; Wang, Y. *Phys. Rev. B* **1992**, *45*, 13244. (b) Perdew, J. P.; Chevary, J. A.; Vosko, S. H.; Jackson, K. A.; Pederson, M. R.; Singh, D. J.; Fiolhais, C. *Phys. Rev. B* **1992**, *46*, 6671.

(14) (a) Blöchl, P. E. *Phys. Rev. B* **1994**, *50*, 17953. (b) Kresse, G.; Joubert, D. *Phys. Rev. B* **1999**, *59*, 1758.

(15) Connelly, N. G.; Damhus, T.; Hartshorn, R. M.; Hutton, A. T. *Nomenclature of Inorganic Chemistry—IUPAC Recommendations 2005*; RSC Publishing: Cambridge, U.K., 2005.

(16) Blatov, V. A.; Proserpio, D. M. V4.0 ed.; Samara, Russia, 2010.

(17) *Infrared and Raman Spectra of Inorganic and Coordination Compounds*, 6th ed.; Nakamoto, K., Ed.; John Wiley & Sons, Inc.: Hoboken, NJ, 2009.

- (18) Zhukov, S. G.; Yatsenko, A.; Chernyshev, V. V.; Trunov, V.; Tserkovnaya, E.; Antson, O.; Hoelsae, J.; Baules, P.; Schenk, H. *Mater. Res. Bull.* **1997**, *32*, 43.
- (19) (a) Lee, C.; Mellot-Draznieks, C.; Slater, B.; Wu, G.; Harrison, W. T. A.; Rao, C. N. R.; Cheetham, A. K. *Chem. Commun.* **2006**, 2687. (b) Gándara, F.; de la Peña-O'Shea, V. c. A.; Illas, F.; Snejko, N.; Proserpio, D. M.; Gutiérrez-Puebla, E.; Monge, M. A. *Inorg. Chem.* **2009**, *48*, 4707. (c) Bernini, M. a. C.; de la Peña-O'Shea, V. A.; Iglesias, M.; Snejko, N.; Gutierrez-Puebla, E.; Brusau, E. V.; Narda, G. E.; Illas, F.; Monge, M. A. n. *Inorg. Chem.* **2010**, *49*, 5063. (d) Platero-Prats, A. E.; de la Peña-O'Shea, V. A.; Proserpio, D. M.; Snejko, N.; Gutiérrez-Puebla, E.; Monge, Á. *J. Am. Chem. Soc.* **2012**, *134*, 4762.
- (20) (a) Tietze, L. F.; Beifuss, U. In *Comprehensive Organic Synthesis*; Barry, M. T., Ian, F., Eds.; Pergamon: Oxford, 1991. (b) Pines, H. *Industrial and Laboratory Alkylations*; American Chemical Society: 1977; Vol. 55.
- (21) (a) Ohmori, O.; Fujita, M. *Chem. Commun.* **2004**, 1586. (b) Hong, D.-Y.; Hwang, Y. K.; Serre, C.; Férey, G.; Chang, J.-S. *Adv. Funct. Mater.* **2009**, *19*, 1537. (c) Horike, S.; Dincă, M.; Tamaki, K.; Long, J. R. *J. Am. Chem. Soc.* **2008**, *130*, 5854. (d) Hasegawa, S.; Horike, S.; Matsuda, R.; Furukawa, S.; Mochizuki, K.; Kinoshita, Y.; Kitagawa, S. *J. Am. Chem. Soc.* **2007**, *129*, 2607.
- (22) Gregory, R. J. H. *Chem. Rev.* **1999**, *99*, 3649.